

Simulating X-ray absorption spectra with CASSCF linear response methods

Benjamin Helmich-Paris *

March 1, 2022

Abstract

In this work, two approaches for simulating X-ray absorption (XA) spectra with the complete active space self-consistent field (CASSCF) linear response (LR) method are introduced. The first approach employs the well-known core-valence separation (CVS) approximation, which is predominantly used by many other electronic structure methods for simulating X-ray spectra. The second ansatz uses the harmonic Davidson algorithm (DA) for finding interior eigenvalues that lie close to a target excitation energy shift and virtually solves a shifted-and-inverted (S&I) generalized eigenvalue problem. Our implementations of these Davidson-type algorithms for core spectroscopies converge as rapidly as the standard DA for valence excitations. It is shown in a proof-of-principle application to the Manganese atom that the additional errors for excitations energies introduced by the CVS approximation compared to the exact S&I approach are negligible for K-edges, but become larger than the methodological error of the CASSCF LR method when computing M-edges. We could also demonstrate that, in case of large active-space K-edge calculations, the computational savings of the CVS approximation are huge as the configuration part of the response vectors is completely neglected. When simulating the oxygen K-edge XA spectrum of the permanganate ion, CASSCF LR showed a better agreement with the experimental spectrum than the CAS-CI and NEVPT2 methods, however, the order of the two close-together pre-edge peaks seems to be inverted.

*Max-Planck-Institut für Kohlenforschung, D-45470 Mülheim an der Ruhr

1 Introduction

In the last decades, the field of theoretical and computational spectroscopy has made enormous progress and allows us today to simulate various types of experimental X-ray spectra.¹ Since the initial work of Bagus in 1965 on core-hole states with Hartree–Fock theory,² many milestones have been reached in the course of time as the core-valence separation (CVS) approximation,³ the maximum overlap method,⁴ real-time propagation approaches,^{5–8} complex polarization propagators,⁹ oscillator strengths beyond the electric dipole approximation,^{10–13} etc.

In particular for transition-metal (TM) compounds X-ray spectroscopy is a frequently used technique that can provide valuable insights into the electronic structure, oxidation and spin state, and coordination number of the metal centers.¹⁴ Those open-shell TM compounds show a characteristic pre-edge peak in the X-ray absorption (XA) spectrum stemming from the excitation of an electron from a core shell into the partially filled TM 3d shell. However, open-shell TM complexes usually have a complicated electronic structure that can only be described properly either by a restricted open-shell ansatz^{15,16} or by multi-reference (MR) methods.^{17–19} The latter are unavoidable when calculating open-shell TM complexes in a low-spin state.

Similar multi-step protocols based on MR methods have been developed by several groups to simulate XA spectra of TM complexes.^{17,19–21} These approaches can be briefly classified into the following four steps: (i) Orbitals for the electronic ground state are obtained from a complete active space self consistent field (CASSCF) calculation either for a single state or for an average of a few low-lying states. Usually, the valence TM d and optionally the attached ligand electrons and orbitals are included in the active space. (ii) Then, a complete or restricted active space (RAS) configuration interaction (CI) calculation is performed for the core-excited states with an active space that has been extended by the desired core electrons and orbitals. In this way, the CVS approximation is easily implemented that restricts the space of CI determinants to those describing excitations from the core into the valence orbital subspace. (iii) In case of L- and M-edge XA spectra, spin-orbit coupling (SOC) must be included for describing the splitting of the 2p and 3p shells, respectively, and

to obtain even qualitatively correct results. Those multi-step approaches usually employ state interactions^{16,22} (SI) of the nonrelativistic core-excited RAS-CI states with different multiplicities that are coupled by an (effective) one-electron SOC perturbation operator^{23,24}. (iv) Dynamic correlation is often introduced by performing MR second-order perturbation theory^{25–31} (PT2) or MR coupled cluster^{32–34} (CC) on top of the many nonrelativistic core-excited RAS-CI wavefunctions. When simulating L- or M-edge spectra, the state energies of such accurate calculations are then incorporated into the SOC SI Hamiltonian by means of diagonal shifts.²²

In recent years, the applicability and accuracy of such type of multi-step approaches has been successfully demonstrated by several computational studies.^{17–21} Nevertheless, it should be mentioned that such multi-step approaches are usually only suited to compute the core-excitation energy fairly accurately. Compromises are made already when computing oscillator strengths or the SOC SI Hamiltonian for which transition or SOC matrix elements are computed at the CASSCF / RAS-CI level. One has to face similar limitation when computing other properties related to core excitations following such multi-step protocols.

The current work focuses on a one-step approach for simulating XA spectra with MR electronic structure methods. Our approach is based on computing core excitation energies and oscillator strengths from the CASSCF linear response (LR) function^{35–39} and builds upon previous work on CASSCF LR valence electron absorption spectra for large molecules.³⁹ With the LR or polarization propagator (PP) ansatz, excitation energies and oscillator strengths are determined from the poles and residues of the LR function,^{37,40} which can be used for simulating valence and core excitations alike. The preference of LR theory over approaches that compute excited states directly by a state averaging and/or CI procedure is justified by (i) higher accuracy due to state-specific eigenvectors representing excited state wavefunctions, (ii) the avoidance of artificial valence-Rydberg mixing with diffuse basis sets, (iii) and the capability of describing excited states that are not exclusively represented by the active space CI determinants. The latter point becomes relevant when simulating the near-edge fine structure of the XA spectrum that, in the one-particle picture, corresponds to electronic excitations from the core into the low-lying unoccupied orbitals. We note at this point that the near K-edge fine structure features of the XA spectra of closed-shell atoms

and small molecules were calculated with impressive accuracy using CC LR theory.⁴¹ Most likely, one can expect a similar accuracy for open-shell systems once highly accurate MR-PT and MR-CC LR methods are available for core excitations.

For single-reference (SR) methods a combination of LR and PP approaches with the CVS approximation is well established and goes back to the early work of Barth and Schirmer⁴² on K-edge spectra using the second-order algebraic diagrammatic construction⁴³ in combination with the CVS approximation.³ Since then, the CVS approximation has been employed along with many SR LR and related methods as CC LR^{41,44} and equation-of-method (EOM) methods,⁴⁵ LR time-dependent density functional theory (DFT),^{6,10,46,47} or the doubles (D) correction to configuration interaction singles (CIS).⁴⁸

Another strategy for determining core excitations with LR approaches is to use modified iterative diagonalization algorithms designed for finding interior eigenvalues of LR eigenvalue equations. In the present work, the harmonic Davidson method of Morgan^{49,50} is employed that searches for all interior eigenvalues close to a target excitation energy shift. Compared to even more sophisticated iterative diagonalization algorithms,^{51–54} only modest adaptations of the original multi-state Davidson algorithm⁵⁵ (DA) for the lowest excitation energies become necessary. The harmonic DA has been employed already in several other fields of electronic structure theory, e.g. for finding a few selected valence bands in solids using Kohn-Sham DFT.^{56,57} Also for density matrix renormalization group methods for quantum chemistry^{58,59}, the harmonic DA is advantageous because the more accurate state-specific ansatz or averaging over fewer states becomes available.

This article shows how the CASSCF LR approach, also known as the multiconfigurational random phase approximation (MC-RPA), can be employed for simulating XA spectra using either the CVS approximation or the harmonic DA. General aspects of CASSCF LR theory with a focus on computing excitation energies are presented in Sec. 2. Moreover, the CVS approximation for MC-RPA calculations and the MC Tamm–Dancoff approximation (MC-TDA) is presented in more detail and key aspects of the harmonic DA for MC-TDA and MC-RPA calculations are covered. After providing technical details on the calculations in Sec. 3, results on proof-of-principle calculations are shown in Sec. 4. Here, we mainly focus on accuracy of the CVS approximation, convergence of the (harmonic) Davidson algorithm, and

accuracy of the MC-RPA method in comparison with other MR methods when be applied for K-edge spectra.

2 Theory

2.1 CASSCF linear response approach

The CASSCF method is a fully variational wavefunction model. For those models, the time-dependent (TD) phase-isolated wavefunction can be obtained from the time-independent wavefunction $|0\rangle$ by unitary transformation.^{36,37,40} Propagating the CASSCF wavefunctions in time is established by unitary transformations of the orbital and configuration part of $|0\rangle$

$$|\tilde{0}\rangle = \exp(\hat{\kappa}(t)) \exp(\hat{S}(t)) |0\rangle. \quad (1)$$

The exponential form of the TD unitary transformations in Eq. 1 demands the exponents to be anti-Hermitian TD operators. The exponent of the orbital part is given by TD orbital rotations that involve single-electron excitation \hat{q}_m^\dagger and deexcitation operators \hat{q}_m ,

$$\hat{\kappa}(t) = \sum_m \left(\kappa_m(t) \hat{q}_m^\dagger - \kappa_m^*(t) \hat{q}_m \right), \quad (2)$$

$$\hat{q}_m^\dagger = \hat{E}_{pq} = \hat{a}_{p\alpha}^\dagger \hat{a}_{q\alpha} + \hat{a}_{p\beta}^\dagger \hat{a}_{q\beta} \quad \text{and} \quad \hat{q}_m = \hat{E}_{qp}, \quad (3)$$

while the exponent of the configuration part involves state-transfer operators \hat{R}_m^\dagger and \hat{R}_m between the time-independent reference state CI wavefunction $|0\rangle$ and the orthogonal complement states $|m\rangle$

$$\hat{S}(t) = \sum_{m>0} \left(S_m(t) \hat{R}_m^\dagger - S_m^*(t) \hat{R}_m \right), \quad (4)$$

$$\hat{R}_m^\dagger = |m\rangle\langle 0| \quad \text{and} \quad \hat{R}_m = |0\rangle\langle m|, \quad (5)$$

that, if combined with $|0\rangle$, form the complete set of CAS-CI configuration state functions (CSF).

In response theory, the external electromagnetic field is treated as time-periodic perturbation.^{37,40,60} Applying the time-dependent variational principle leads in second order in the

perturbation strengths to the generalized eigenvalue equations

$$\mathbf{E}^{(2)} \mathbf{X} = \omega \mathbf{S}^{(2)} \mathbf{X} \quad (6)$$

that involve the electronic Hessian $\mathbf{E}^{(2)}$ and a generalized metric $\mathbf{S}^{(2)}$ matrices. The solution of Eq. 6 gives the poles of the CASSCF linear response function ω , which can be identified as excitation energies in an exact theory.^{37,40} The duality of excitation and deexcitation operators to create anti-Hermitian operators $\hat{\kappa}(t)$ and $\hat{S}(t)$ leads to a two-by-two block structure of the $\mathbf{E}^{(2)}$ and $\mathbf{S}^{(2)}$ matrices,

$$\begin{pmatrix} \mathbf{A} & \mathbf{B} \\ \mathbf{B}^* & \mathbf{A}^* \end{pmatrix} \begin{pmatrix} \mathbf{Z} \\ \mathbf{Y}^* \end{pmatrix} = \omega \begin{pmatrix} \mathbf{\Sigma} & \mathbf{\Delta} \\ -\mathbf{\Delta}^* & -\mathbf{\Sigma}^* \end{pmatrix} \begin{pmatrix} \mathbf{Z} \\ \mathbf{Y}^* \end{pmatrix}. \quad (7)$$

Due to block structure of Eq. 7, there are two different solutions of the eigenvalue problem

$$\begin{aligned} +\omega \quad \text{and} \quad \mathbf{X}(+\omega) &= \begin{pmatrix} \mathbf{Z} \\ \mathbf{Y}^* \end{pmatrix}, \\ -\omega \quad \text{and} \quad \mathbf{X}(-\omega) &= \begin{pmatrix} \mathbf{Y} \\ \mathbf{Z}^* \end{pmatrix}, \end{aligned} \quad (8)$$

representing electronic excitations and de-excitations, respectively. In order to not break the paired structure of these RPA-type eigenvalue problems both solutions need to be determined simultaneously. Alternatively, linear (plus and minus) combinations of the eigenvectors $\mathbf{X}(\omega)$ and $\mathbf{X}(-\omega)$,

$$\mathbf{U}(h) = \mathbf{X}(+\omega) + h \mathbf{X}(-\omega) = \begin{pmatrix} \mathbf{Z} + h \mathbf{Y} \\ \mathbf{Y}^* + h \mathbf{Z}^* \end{pmatrix} = \begin{pmatrix} \mathbf{V} \\ h \mathbf{V}^* \end{pmatrix}, \quad (9)$$

can be determined rather than the eigenvectors themselves, which is known as the Hermitian ($+h$) and anti-Hermitian ($-h$) form of the eigenvectors introduced by Saue and Jensen.⁶¹

In practice, we are only interested in a few roots of the LR eigenvalue problem, which are determined iteratively by Davidson-type algorithms.⁵⁵ For such iterative diagonalization algorithms, products of a few trial vectors \mathbf{b} with the large matrices $\mathbf{E}^{(2)}$ and $\mathbf{S}^{(2)}$ of Eq. 6 need to be computed. As was shown originally by Saue and Jensen,^{39,61} the Hermiticity of the Hermitian ($h = +1$) and anti-Hermitian ($h = -1$) trial vectors is conserved when being

multiplied with the Hermitian $\mathbf{E}^{(2)}$ matrix,

$$\begin{pmatrix} \mathbf{A} & \mathbf{B} \\ \mathbf{B}^* & \mathbf{A}^* \end{pmatrix} \begin{pmatrix} \mathbf{b} \\ h \mathbf{b}^* \end{pmatrix} = \begin{pmatrix} \mathbf{A}\mathbf{b} + h \mathbf{B}\mathbf{b}^* \\ h (\mathbf{A}\mathbf{b} + h \mathbf{B}\mathbf{b}^*) \end{pmatrix} = \boldsymbol{\sigma}_{(h)} \quad (10)$$

and inverted when being multiplied with the anti-Hermitian $\mathbf{S}^{(2)}$ matrix

$$\begin{pmatrix} \boldsymbol{\Sigma} & \boldsymbol{\Delta} \\ -\boldsymbol{\Delta}^* & -\boldsymbol{\Sigma}^* \end{pmatrix} \begin{pmatrix} \mathbf{b} \\ h \mathbf{b}^* \end{pmatrix} = \begin{pmatrix} \boldsymbol{\Sigma}\mathbf{b} + h \boldsymbol{\Delta}\mathbf{b}^* \\ -h (\boldsymbol{\Sigma}\mathbf{b} + h \boldsymbol{\Delta}\mathbf{b}^*) \end{pmatrix} = \boldsymbol{\tau}_{(-h)}, \quad (11)$$

As becomes apparent from Eqs. 10 and 11, only one component (upper or lower) of the (anti-)Hermitian trial vectors \mathbf{b} and linearly transformed trial vectors $\boldsymbol{\sigma}$ and $\boldsymbol{\tau}$ is sufficient. We choose the upper component without loss of generality. If needed, the redundant lower component is readily available by complex conjugation and an additional phase change for anti-Hermitian vectors.

One of the advantages of exploiting Hermiticity emerges when computing vector products. If two vectors with the same Hermiticity ($h_1 = h_2$) are multiplied, their product is purely real; if two vectors with different Hermiticity ($h_1 \neq h_2$) are multiplied, their product is purely imaginary,

$$\mathbf{U}_{1,(h_1)}^\dagger \mathbf{U}_{2,(h_2)} = \mathbf{V}_1^\dagger \mathbf{V}_2 + h_1 h_2 (\mathbf{V}_1^\dagger \mathbf{V}_2)^*, \quad (12)$$

$$= \begin{cases} 2 \operatorname{Re}(\mathbf{V}_1^T \mathbf{V}_2) & \text{if } h_1 = h_2 \\ 2i \operatorname{Im}(\mathbf{V}_1^T \mathbf{V}_2) & \text{if } h_1 \neq h_2 \end{cases}. \quad (13)$$

This becomes relevant when formulating the MC-RPA eigenvalue problem, Eq. 7, in the reduced space spanned by the trial vectors \mathbf{b} . Since we are dealing only with real quantities when solving the LR eigenvalue equations for non-relativistic Hamiltonians, two out of the four blocks of the reduced space $\mathbf{E}^{[2]}$ and $\mathbf{S}^{[2]}$ matrices vanish

$$\begin{pmatrix} \mathbf{b}_{(+)}^\dagger \boldsymbol{\sigma}_{(+)} & 0 \\ 0 & \mathbf{b}_{(-)}^\dagger \boldsymbol{\sigma}_{(-)} \end{pmatrix} \begin{pmatrix} \mathbf{u}_{(+)} \\ \mathbf{u}_{(-)} \end{pmatrix} = \omega_i \begin{pmatrix} 0 & \mathbf{b}_{(+)}^\dagger \boldsymbol{\tau}_{(+)} \\ \mathbf{b}_{(-)}^\dagger \boldsymbol{\tau}_{(-)} & 0 \end{pmatrix} \begin{pmatrix} \mathbf{u}_{(+)} \\ \mathbf{u}_{(-)} \end{pmatrix}. \quad (14)$$

In a previous work on UV/Vis absorption spectra with the MC-RPA method,³⁹ this Hermiticity-block structure was exploited and led to substantial computational savings if many roots are optimized simultaneously.

2.2 Core-valence separation approximation

The sub-blocks of $\mathbf{E}^{(2)}$ and $\mathbf{S}^{(2)}$ appearing in Eq. 7 can be decomposed further according to their operator types in the wavefunction model. In case of CASSCF-type wavefunction models, there is in turn a two-by-two block structure when separating the orbital $\hat{\kappa}$ and configuration \hat{S} rotation part in the super matrices \mathbf{A} , \mathbf{B} , $\mathbf{\Sigma}$, and $\mathbf{\Delta}$,

$$\begin{aligned} A_{ij} &= \begin{pmatrix} \langle 0 | [\hat{q}_i, [\hat{H}, \hat{q}_j^\dagger]] | 0 \rangle & \langle 0 | [\hat{q}_i, [\hat{H}, \hat{R}_j^\dagger]] | 0 \rangle \\ \langle 0 | [\hat{R}_i, [\hat{H}, \hat{q}_j^\dagger]] | 0 \rangle & \langle 0 | [\hat{R}_i, [\hat{H}, \hat{R}_j^\dagger]] | 0 \rangle \end{pmatrix}, \\ B_{ij} &= \begin{pmatrix} \langle 0 | [q_i, [\hat{H}, q_j]] | 0 \rangle & \langle 0 | [q_i, [\hat{H}, R_j]] | 0 \rangle \\ \langle 0 | [R_i, [\hat{H}, q_j]] | 0 \rangle & \langle 0 | [R_i, [\hat{H}, R_j]] | 0 \rangle \end{pmatrix}, \\ \Sigma_{ij} &= \begin{pmatrix} \langle 0 | [q_i, q_j^\dagger] | 0 \rangle & \langle 0 | [q_i, R_j^\dagger] | 0 \rangle \\ \langle 0 | [R_i, q_j^\dagger] | 0 \rangle & \langle 0 | [R_i, R_j^\dagger] | 0 \rangle \end{pmatrix}, \\ \Delta_{ij} &= \begin{pmatrix} \langle 0 | [q_i, q_j] | 0 \rangle & \langle 0 | [q_i, R_j] | 0 \rangle \\ \langle 0 | [R_i, q_j] | 0 \rangle & \langle 0 | [R_i, R_j] | 0 \rangle \end{pmatrix}. \end{aligned} \tag{15}$$

The structure of the Hessian matrices \mathbf{A} (or \mathbf{B}) is shown schematically in Fig. 1. The orbital-orbital block can be decomposed further into the three possible types of single-particle excitations between the inactive occupied (O), active (A), and virtual (V) MO spaces. All Hessian matrix blocks have nonvanishing elements.

Excitation energies associated with an excitation from the core into the partially occupied active or unoccupied virtual orbitals occur as interior eigenvalues of the Hessian spectrum. For molecular systems with a decent basis set size it is computationally intractable to find those eigenvalues by a full or iterative diagonalization of the full Hessian (and generalized metric) matrix.

A well-established strategy for obtaining XA spectra with LR or PP methods is to restrict the search space to only those vector elements that have a few application-relevant core orbitals. In most cases, coupling of the core and valence part is usually weak and is, thus, neglected within this so-called CVS approximation.

The CVS CASSCF Hessian (and generalized metric) matrix only has non-vanishing elements in the virtual-occupied (V–O) and active-occupied (A–O) orbital part. Only elements with one of the selected core orbitals enter the V–O and A–O blocks. The configuration

part is neglected completely because we assume that for one-step MR LR or PP approaches the active space usually comprises valence orbitals only. The block structure of the CVS CASSCF Hessian is illustrated in Fig. 2. The energetically lowest eigenvalues of the CVS CASSCF Hessian and metric correspond altogether to core excitations and can be easily found by the same DA used for valence excited states (see Sec. 2.1). Note that the computational costs for diagonalizing the CVS CASSCF Hessian and generalized metric can be significantly smaller in cases of larger active spaces as will be demonstrated in Sec. 4.

2.3 Harmonic Davidson Algorithm for high-lying roots

An alternative approach for finding high-lying roots is to employ a modified variant of the DA⁵⁵. The so-called harmonic DA^{49,50} is able to find a desired number of target roots in the vicinity of a user-given excitation energy shift s . In contrast to the CVS ansatz, no additional approximation is introduced here.

2.3.1 MC-TDA

The harmonic Davidson (and interior Jacobi-Davidson) algorithm for solving the generalized eigenvalue problem of symmetric matrices has been described previously, primarily in the field of solid-state electronic structure theory.^{56,57} All relevant points to find interior eigenvalues of the MC-TDA eigenvalue problem are repeated in the following.

To find all interior eigenvalues that are close to shift s , we start with the shifted eigenvalue problem⁵⁶

$$(\mathbf{A} - s\mathbf{\Sigma})\mathbf{X} = (\omega - s)\mathbf{\Sigma}\mathbf{X} \quad (16)$$

$$\tilde{\mathbf{A}}\mathbf{X} = \tilde{\omega}\mathbf{\Sigma}\mathbf{X}. \quad (17)$$

In the iterative Davidson-type algorithms, the eigenvectors

$$\mathbf{X} = \mathbf{P} \mathbf{u} \quad (18)$$

are expanded in set of M trial vectors $\mathbf{P} = [\mathbf{b}_1, \mathbf{b}_2, \dots, \mathbf{b}_M]$. This so-called reduced space is expanded in every iteration such that the approximate eigenvectors in Eq. 18 converge quickly towards the exact solution.

For the harmonic DA, the shifted eigenvalue problem, Eq. 17, is projected by a different set of trail vectors \mathbf{Q} from the left

$$\mathbf{Q}^\dagger \tilde{\mathbf{A}} \mathbf{P} \mathbf{u} = \tilde{\omega} \mathbf{Q}^\dagger \Sigma \mathbf{P} \mathbf{u} \quad (19)$$

$$\mathbf{Q} = \tilde{\mathbf{A}} \mathbf{P}. \quad (20)$$

Eq. 19 can be expressed entirely in terms of the nonorthogonal \mathbf{Q} vectors, which leads to a shifted and inverted (S&I) formulation of the generalized eigenvalue problem,

$$\mathbf{Q}^\dagger \Sigma \tilde{\mathbf{A}}^{-1} \mathbf{Q} \mathbf{u} = \frac{1}{\tilde{\omega}} \mathbf{Q}^\dagger \mathbf{Q} \mathbf{u} \quad (21)$$

$$\mathbf{Q}^\dagger \Sigma \mathbf{P} \mathbf{u} = \alpha \mathbf{Q}^\dagger \mathbf{Q} \mathbf{u}. \quad (22)$$

By inspecting Eq. 22, it is clear that no costly inversion or any solution of a linear system of equations is ever required.

For reasons that will become apparent later, the S&I MC-TDA eigenvalue equations in the reduced space, Eq. 22, are formulated in terms of linearly transformed Hessian and generalized metric vectors $\boldsymbol{\sigma}$ and $\boldsymbol{\tau}$

$$\mathbf{H}^{\text{TDA}} \mathbf{u}_i = \alpha_i \mathbf{S}^{\text{TDA}} \mathbf{u}_i \quad (23)$$

$$H_{ij}^{\text{TDA}} = \boldsymbol{\sigma}_i^\dagger \boldsymbol{\tau}_j - s \boldsymbol{\tau}_i^\dagger \boldsymbol{\tau}_j \quad (24)$$

$$S_{ij}^{\text{TDA}} = \boldsymbol{\sigma}_i^\dagger \boldsymbol{\sigma}_j - s (\boldsymbol{\tau}_i^\dagger \boldsymbol{\sigma}_j + \boldsymbol{\sigma}_i^\dagger \boldsymbol{\tau}_j) - s^2 \boldsymbol{\tau}_i^\dagger \boldsymbol{\tau}_j \quad (25)$$

To find all those roots that are close to s , only those eigenvectors \mathbf{u}_i are considered that have the largest absolute value $|\alpha_i|$ amongst all M current reduced-space eigenvalues. As illustrated in Fig. 3, the original eigenvalues that were located formerly in the interior of the spectrum (close to s) become exterior eigenvalues of the S&I eigenvalue equations and can be determined by Davidson-type algorithms.

We should note that the reduced-space matrix \mathbf{H}^{TDA} is non-symmetric and, thus, complex eigenvalues and eigenvectors may occur in course of the DA. Nevertheless, the eigenvalues of the untransformed MC-TDA eigenvalue equations must be real. If complex roots occur, we follow the approach of Ref. 57 and simply take their absolute values. Upon convergence, complex roots cannot occur anymore, at least amongst the set of request target roots.

Another difference between the harmonic and the standard DA for the MC-TDA generalized eigenvalue equations is that the Rayleigh quotient

$$\rho_i = \frac{\mathbf{x}_i^\dagger \mathbf{A} \mathbf{x}_i}{\mathbf{x}_i^\dagger \mathbf{\Sigma} \mathbf{x}_i} \quad (26)$$

is not equal to the (harmonic) Ritz values $\theta_i = s + 1/\alpha_i$ before convergence is reached. This is because the eigenvectors \mathbf{X} are expanded in the set of \mathbf{P} vectors rather than \mathbf{Q} vectors. However, the latter are used for the S&I MC-TDA eigenvalue problem in the reduced space, Eq. 21.⁵⁰ Thus, in our implementation ρ_i is computed as

$$\rho_i = \frac{\mathbf{x}_i^\dagger \boldsymbol{\sigma}_i}{\mathbf{x}_i^\dagger \boldsymbol{\tau}_i} \quad (27)$$

after expanding the (linearly transformed) trial vectors \mathbf{b} , $\boldsymbol{\sigma}$, and $\boldsymbol{\tau}$ into the full space. Accordingly, the residual vector of every target root is computed from ρ_i

$$\mathbf{r}_i = \boldsymbol{\sigma}_i - \rho_i \boldsymbol{\tau}_i \quad (28)$$

Trial vectors for the next iteration of the harmonic DA are selected and preconditioned as for the standard DA briefly described in Sec. 2.1 or elsewhere.³⁹

2.3.2 MC-RPA

Adapting the harmonic DA for RPA-type generalized eigenvalue problems is less straightforward because of the diametrical symmetry properties of the $\boldsymbol{\sigma}$ and $\boldsymbol{\tau}$ vectors that are needed for left projection with \mathbf{Q} . As shown in Eqs. 10 and 11, $\boldsymbol{\sigma}$ vectors preserve the Hermiticity h of the corresponding trial vectors b while $\boldsymbol{\tau}$ invert h .

Let us start with the shifted (MC-)RPA eigenvalue equations for which the eigenvectors \mathbf{X} are expanded in a set of trial vectors

$$\begin{pmatrix} \boldsymbol{\sigma}_{(+)} & -s \boldsymbol{\tau}_{(+)} \\ -s \boldsymbol{\tau}_{(-)} & \boldsymbol{\sigma}_{(-)} \end{pmatrix} \begin{pmatrix} \mathbf{u}_{(+)} \\ \mathbf{u}_{(-)} \end{pmatrix} = (\omega - s) \begin{pmatrix} 0 & -s \boldsymbol{\tau}_{(+)} \\ -s \boldsymbol{\tau}_{(-)} & 0 \end{pmatrix} \begin{pmatrix} \mathbf{u}_{(+)} \\ \mathbf{u}_{(-)} \end{pmatrix} \quad (29)$$

The matrix at the left-hand side of Eq. 29 can be readily identified as the left projector

$$\mathbf{Q} = \begin{pmatrix} \boldsymbol{\sigma}_{(+)} & -s \boldsymbol{\tau}_{(+)} \\ -s \boldsymbol{\tau}_{(-)} & \boldsymbol{\sigma}_{(-)} \end{pmatrix} \quad (30)$$

which features a 2-by-2 block structure determined by Hermiticity. Projecting the shifted MC-RPA equation, Eq. 29, from the left with \mathbf{Q} leads to the following generalized RPA-type eigenvalue problem in the reduced space

$$\mathbf{H}^{\text{RPA}} \begin{pmatrix} \mathbf{u}_{(+)} \\ \mathbf{u}_{(-)} \end{pmatrix} = \alpha_i \mathbf{S}^{\text{RPA}} \begin{pmatrix} \mathbf{u}_{(+)} \\ \mathbf{u}_{(-)} \end{pmatrix} \quad (31)$$

$$H_{ij}^{\text{RPA}} = \begin{pmatrix} -s \tau_{(-),i}^{\dagger} \tau_{(-),j} & \sigma_{(+),i}^{\dagger} \tau_{(+),j} \\ \sigma_{(-),i}^{\dagger} \tau_{(-),j} & -s \tau_{(+),i}^{\dagger} \tau_{(+),j} \end{pmatrix} \quad (32)$$

$$S_{ij}^{\text{RPA}} = \begin{pmatrix} \sigma_{(+),i}^{\dagger} \sigma_{(+),j} + s^2 \tau_{(-),i}^{\dagger} \tau_{(-),j} & -s \left(\sigma_{(+),i}^{\dagger} \tau_{(+),j} + \tau_{(-),i}^{\dagger} \sigma_{(-),j} \right) \\ -s \left(\tau_{(+),i}^{\dagger} \sigma_{(+),j} + \sigma_{(-),i}^{\dagger} \tau_{(-),j} \right) & \sigma_{(-),i}^{\dagger} \sigma_{(-),j} + s^2 \tau_{(+),i}^{\dagger} \tau_{(+),j} \end{pmatrix} \quad (33)$$

that is solved in every iteration of in the harmonic DA.

In contrast to the generalized RPA eigenvalue problem that is solved with the standard DA, Eq. 14, non of the Hermiticity blocks vanishes in the eigenvalue equations 31. Thus, the computational costs for solving Eq. 31 are much higher than those of Eq. 14. However, for most applications only it is sufficient to find only a few roots and, thus, the costs for calculating the MC-RPA sigma vectors are usually much higher than those for solving the eigenvalue equations in the reduced space.

The reduced-space matrix \mathbf{H}^{RPA} is non-symmetric as in the MC-TDA case and, again, complex eigenvalue may occur.

3 Computational Details

All calculations were performed with a development version of ORCA - an *ab initio*, DFT and semi-empirical SCF-MO package.^{62,63} The CVS approximation and the harmonic DA have been implemented in the `orca_mcrpa` module.³⁹ More technical details on `orca_mcrpa` can be found in Ref. 39. The energy shift used for the S&I approach was derived from other calculations or experimental values. Please note that the exact value of the shift is not relevant. Taking a slightly different shift will at most lead to shifting the energy window range of the converged roots. If many roots are requested, as it is usually the case when

simulating UV/Vis and XAS spectra, a slight shift in the energy window should be of no concern.

All core orbitals were considered in the calculations whenever the CVS approximation was not used. To account for scalar-relativistic effects, we employed the spin-free second-order Douglas–Kroll–Hess (DKH2) Hamiltonian.^{64,65} For all DFT calculations we used the B3LYP exchange-correlation functional^{66–68} and the unrestricted Kohn-Sham ansatz. In the subsequent TD-DFT calculation the CVS approximation was applied, i.e. the orbital window for the occupied orbitals was restricted to a specific set of core orbitals.

The RI approximation has been used for all MR methods. The auxiliary basis set was automatically generated by the AutoAux program available in ORCA.⁶⁹

Note that we have used the electric dipole approximation when computing oscillator strengths for all XA spectra.

For reasons of consistency with the study of Chantzis *et al.*,²⁰ the uncontracted cc-pVTZ basis set⁷⁰ was used for all calculations on the Manganese atom. For the CASSCF ground state energy and MC-RPA calculations on Manganese, a CAS with five electrons in five (d) orbitals in a sextet state was chosen. The CAS-CI and NEVPT2^{28–30} results were obtained as described in Ref. 20, i.e. the 1s, 2p, or 3p core orbitals, respectively, of the CAS-(5,5)-SCF calculation were rotated right below the active 3d orbitals; then the active space was augmented by the core electrons and orbitals (CAS(7,6) for K-edge, CAS(11,8) for L- and M-edge) in the succeeding CAS-CI and NEVPT2 calculation. The strongly-contracted NEVPT2 variant was employed in this study. While the CVS CAS-CI calculation reuses the CAS-(5,5)-SCF without any modification, in NEVPT2 the MOs get canonicalized for each state by diagonalizing the state-specific total Fock matrix \mathbf{F} that depends on the CAS-CI solution vector in its active part.⁷¹

For all calculations on the permanganate ion MnO_4^- , a perfect tetrahedral structure was assumed with an experimental bond length of 1.629 Å.⁷² A customized version of the def2-QZVPP basis set⁷³ was used with special contraction coefficients for the DKH2 Hamiltonian.⁷⁴ An active space with all Mn 3d and all O 2p electrons and orbitals, CAS (24,17), was chosen for all the CASSCF and MC-RPA calculations. A different active space, CAS(8,9), was employed for the CVS CAS-CI and NEVPT2 calculations that contains all O 1s and

the Mn 3d electrons and orbitals. Those calculations used the orbitals from the preceding CAS-(24,17)-SCF calculation. We have again used state-specific canonical orbitals as for the Manganese calculations.

4 Results and discussion

4.1 Accuracy of the CVS approximation

The accuracy of the CVS approximation is investigated for the K-, L-, and M-edge transition of the Manganese atom. Those transition are dominated by a one-electron promotion from the 1s (K), 2p (L), and 3p (M) core shell into the half-filled valence 3d shell. The MC-RPA excitation energies for those transitions are compiled in Tab. 1 along with the TD-DFT B3LYP, CAS-CI, and NEVPT2 results. Excitation energies are provided as differences to the NEVPT2 results. Note that only for the K-edge an experimental reference is provided. A realistic simulation and assignment of L- and M-edge spectra⁷⁵ requires inclusion of spin-orbit coupling due to the pronounced splitting of core p shells, which is currently not available, at least, for the CASSCF LR implementation.

As can be seen from Tab. 1, the transition energies from the CASSCF type methods, i.e. CAS-CI, CVS MC-RPA and S&I MC-RPA, are systematically blue shifted, while those from CVS TD-DFT are systematically too small. This trend is fully in line with benchmark results on valence excitations energies⁷⁶ and can be readily attributed to an insufficient treatment of dynamic electron correlation.

Much more interesting is the accuracy of the CVS approximation in comparison to the exact S&I approach for high-lying MC-RPA excitation energies. In case of K-edge transitions, which involve single-electron excitations from the lowest 1s orbital, the difference between CVS and S&I is roughly 10^{-4} eV and many orders of magnitude below the inherent error of the electronic structure method or the basis set incompleteness error.

A completely different observation can be made for the M-edge spectra for which electrons in the 3p shell get promoted into the valence 3d shell. These excitations occur in the presence of electromagnetic radiation from UV part of the light spectrum rather than the (soft) X-ray

part. For those transitions, we observe a complete breakdown of the CVS approximation. CVS and S&I MC-RPA excitation energies differ by up to 3.5 eV, which is twice as large as the energetic difference to the NEVPT2 results. Though exhaustive benchmarking was not made in the current study, we may conclude that CVS is an excellent approximation for K-edge transitions. In case of transitions induced by UV or low-energy X-ray radiation the S&I approach based on the harmonic DA has to be used to prevent severe errors.

4.2 O K-edge XAS of MnO_4^-

To demonstrate the feasibility of MC-RPA for simulating XAS spectra of molecular systems, the oxygen pre- and near K-edge XA was simulated by computing 50 roots using either the CVS approximation or the S&I approach with a shift of 530 eV. With both Davidson-type implementations (standard and harmonic DA) the Frobenius norms $\|\mathbf{r}\|$ of the residual vectors, Eq. 28, converged smoothly below a threshold of 10^{-4} within 8 and 11 iterations, respectively, as shown in Fig. 4. Interestingly, the S&I algorithm converges faster though the search space for the eigenvectors is much larger. Note that the curve flattening of the minimum and average $\|\mathbf{r}\|$ near convergence is not a sign of convergence issues, but rather caused by an increasing number of converged eigenpairs that are then locked by the DA and not improved further.

Concerning the accuracy of the two approaches, the errors introduced by the CVS approximation are well below 0.1 eV for all roots and irrelevant for any practical purpose. Note that a much more significant deviation between the CVS approximation and the exact S&I approach will most likely be observed when simulating L- and M-edge spectra as seen in Sec. 4.1. The computational savings due to the CVS approximation are huge for such a large active space CAS(24,17) MC-RPA calculation that expands the configuration part of the eigenvectors in more than 8.8×10^6 CSFs. In case of CVS MC-RPA, only the CI problem of the ground must be solved and the calculation completed after 30 min using 20 MPI processes on an Intel Haswell node (Intel® Xeon® CPU E5-2687W v3 @ 3.10 GHz). Conversely, it took roughly 17 h using 24 MPI processes on an Intel Broadwell node (Intel® Xeon® CPU E5-2687W v4 @ 3.00 GHz) until the S&I MC-RPA calculation finished. For the S&I MC-RPA calculation each vector is expanded in the complete space of orbital rotations

and CSFs. When considering both accuracy and efficiency, the CVS approximation should be clearly preferred to the S&I approach for CASSCF LR K-edge spectra.

The O K-edge XAS MC-RPA spectrum (S&I) of MnO_4^- is shown in the top panel of Fig. 5. The two characteristic pre-edge peaks correspond to a transition from the O 1s orbitals into the empty t_2^* and e^* orbitals. Peaks with higher energy in the MC-RPA spectrum belong to the near-edge fine structure region that have so far not been reported by experimental studies. In comparison to the known experimental values of the K pre-edge region,⁷⁷ the two MC-RPA peaks are blueshifted by roughly 10.5 eV. The splitting of the two peaks of 0.85 eV is too small compared to the experimental value of 1.50 eV. Furthermore, our assignment of the K pre-edge peaks in the MC-RPA spectrum contradicts the assignment made in the experimental study of Ref. 77. In our MC-RPA calculation, transitions into the t_2^* orbitals are energetically below the transitions into the e^* orbitals, which seems non-physical for a tetrahedrally coordinated TM complex. Still, a physically sound orbital ordering is revealed when inspecting the CAS-(24,17)-SCF orbital coefficients and pseudo orbital energies. Thus, we suspect a wrong ordering of the MC-RPA pre-edge transitions caused by the lack of dynamical electron correlation rather than a wrong interpretation made in the experimental study of Ref. 77. The presumption is supported when considering the CAS-CI and NEVPT2 K-edge XA spectrum presented in the middle and lower panel of Fig. 5, respectively. While the O 1s $\rightarrow t_2^*$ transition is slightly below the one of O 1s $\rightarrow e^*$ for the CAS-(8,9)-CI calculation, the physically sound ordering in accordance with the ligand-field picture of tetrahedrally coordinated TM complexes is observed in the NEVPT2 calculation. Though the ordering seems to be correct in the NEVPT XA spectrum, the transition energies are significantly redshifted and feature a much larger absolute deviation from the experimental peaks than with MC-RPA. Furthermore, those state-specific NEVPT2 calculations show a significant splitting of the O 1s $\rightarrow e^*$ and O 1s $\rightarrow t_2^*$, which seems to be unphysical and not in line with the experimental spectrum of Ref. 77. Nevertheless, our MC-RPA XA spectrum gave the least deviation from the experimental spectrum except of the questionable ordering of the two pre-edge peaks. We have faith that future computational studies with more accurate MR electronic structure methods will improve the agreement between theory and experiment.

5 Conclusions

In the present work, we have introduced two approaches for simulating XA spectra with the CASSCF LR method also known as MC-RPA. The first approach employs the well-known CVS approximation, which is predominantly used by other electronic structure methods for simulating X-ray spectra. The second ansatz (S&I) uses the harmonic DA for interior eigenvalues that lie close to a user-given shift. Similar algorithms for interior eigenvalues were used already in the context of computational XAS for SR methods as TD-DFT⁵⁴ and EOM-CC⁵³, but not yet for MR LR approaches.

Both implementations of the corresponding Davidson-type algorithm show fast convergence. Even faster convergence is observed for the harmonic DA S&I MC-RPA method for the cases considered in this work.

Furthermore, we could show in a proof-of-principle application to the Manganese atom that the additional errors for excitations energies introduced by the CVS approximation compared to the exact S&I approach are negligible for K-edges, but become larger than the methodological error of the MC-RPA method when computing M-edges. Hence, whenever simulating M-edge spectra, the S&I approach becomes unavoidable.

Nevertheless, in case of large active-space K-edge calculations, the computational savings of the CVS approximation are huge as the configuration part of the response vectors is completely neglected. For such calculations, the CVS approximations should be employed.

The O K-edge XA spectrum of MnO_4^- was simulated with three MR methods, i.e. our one-step MC-RPA approach and the multi-step CAS-CI / NEVPT2 methods. For all those three MR methods, MC-RPA showed the best agreement with the experimental spectrum. However, the order of the two computed pre-edge peaks seems to be questionable. We suspect that MR LR methods that can account for dynamic correlation^{78,79} could provide an even better agreement with the experimental spectrum.

Future developments will focus mainly on the following aspects: (i) inclusion of dynamic correlation to obtain higher accuracy, (ii) treatment of degenerate open-shell ground states that suffer from symmetry breaking, (iii) and the inclusion of spin-orbit coupling to simulate L- and M-edge spectra. Currently, we are working actively on the first two aspects in our

laboratory.

6 Acknowledgments

The author thanks cordially Frank Neese, Dimitrios Manganas, and Mihail Atanasov for fruitful discussions.

7 Funding Information

Financial support by the Max Planck society is gratefully acknowledged.

References

1. P. Norman and A. Dreuw, Chem. Rev. **118**, 7208 (2018), URL <https://doi.org/10.1021/acs.chemrev.8b00156>.
2. P. S. Bagus, Phys. Rev. **139**, A619 (1965), URL <https://link.aps.org/doi/10.1103/PhysRev.139.A619>.
3. L. S. Cederbaum, W. Domcke, and J. Schirmer, Phys. Rev. A **22**, 206 (1980), URL <https://link.aps.org/doi/10.1103/PhysRevA.22.206>.
4. A. T. B. Gilbert, N. A. Besley, and P. M. W. Gill, J. Phys. Chem. A **112**, 13164 (2008), URL <https://doi.org/10.1021/jp801738f>.
5. T. Akama and H. Nakai, J. Chem. Phys. **132**, 054104 (2010), URL <https://doi.org/10.1063/1.3300127>.
6. K. Lopata, B. E. Van Kuiken, M. Khalil, and N. Govind, J. Chem. Theory Comput. **8**, 3284 (2012), URL <https://doi.org/10.1021/ct3005613>.
7. M. Kadek, L. Konecny, B. Gao, M. Repisky, and K. Ruud, Phys. Chem. Chem. Phys. **17**, 22566 (2015), URL <http://dx.doi.org/10.1039/C5CP03712C>.
8. M. Repisky, L. Konecny, M. Kadek, S. Komorovsky, O. L. Malkin, V. G. Malkin, and K. Ruud, J. Chem. Theory Comput. **11**, 980 (2015), URL <http://dx.doi.org/10.1021/ct501078d>.
9. P. Norman, D. M. Bishop, H. J. A. Jensen, and J. Oddershede, J. Chem. Phys. **123**, 194103 (2005), URL <https://doi.org/10.1063/1.2107627>.
10. S. DeBeer George, T. Petrenko, and F. Neese, J. Phys. Chem. A **112**, 12936 (2008), URL <https://doi.org/10.1021/jp803174m>.
11. S. Bernadotte, A. J. Atkins, and C. R. Jacob, J. Chem. Phys. **137**, 204106 (2012), URL <https://doi.org/10.1063/1.4766359>.

12. N. H. List, J. Kauczor, T. Saue, H. J. A. Jensen, and P. Norman, *J. Chem. Phys.* **142**, 244111 (2015), URL <https://doi.org/10.1063/1.4922697>.
13. L. K. Sørensen, E. Kieri, S. Srivastav, M. Lundberg, and R. Lindh, *Phys. Rev. A* **99**, 013419 (2019), URL <https://link.aps.org/doi/10.1103/PhysRevA.99.013419>.
14. J. H. Sinfelt and G. D. Meitzner, *Accounts Chem. Res.* **26**, 1 (1993), URL <https://doi.org/10.1021/ar00025a001>.
15. M. Roemelt and F. Neese, *J. Phys. Chem. A* **117**, 3069 (2013), URL <https://doi.org/10.1021/jp3126126>.
16. M. Roemelt, D. Maganas, S. DeBeer, and F. Neese, *J. Chem. Phys.* **138**, 204101 (2013), URL <https://doi.org/10.1063/1.4804607>.
17. I. Josefsson, K. Kunnus, S. Schreck, A. Föhlisch, F. de Groot, P. Wernet, and M. Odelius, *J. Phys. Chem. Lett.* **3**, 3565 (2012), URL <https://doi.org/10.1021/jz301479j>.
18. K. Kunnus, I. Josefsson, S. Schreck, W. Quevedo, P. S. Miedema, S. Techert, F. M. F. de Groot, M. Odelius, P. Wernet, and A. Föhlisch, *J. Phys. Chem. B* **117**, 16512 (2013), URL <https://doi.org/10.1021/jp4100813>.
19. R. V. Pinjari, M. G. Delcey, M. Guo, M. Odelius, and M. Lundberg, *J. Chem. Phys.* **141**, 124116 (2014), URL <https://doi.org/10.1063/1.4896373>.
20. A. Chantzis, J. K. Kowalska, D. Maganas, S. DeBeer, and F. Neese, *J. Chem. Theory Comput.* **14**, 3686 (2018), URL <https://doi.org/10.1021/acs.jctc.8b00249>.
21. D. Maganas, J. K. Kowalska, M. Nooijen, S. DeBeer, and F. Neese, *J. Chem. Phys.* **150**, 104106 (2019), URL <https://doi.org/10.1063/1.5051613>.
22. P.-Å. Malmqvist, B. O. Roos, and B. Schimmelpfennig, *Chem. Phys. Lett.* **357**, 230 (2002), URL <http://www.sciencedirect.com/science/article/pii/S0009261402004980>.

23. B. A. Heß, C. M. Marian, U. Wahlgren, and O. Gropen, *Chem. Phys. Lett.* **251**, 365 (1996), URL <http://www.sciencedirect.com/science/article/pii/0009261496001194>.
24. B. Schimmelpfennig, L. Maron, U. Wahlgren, C. Teichteil, H. Fagerli, and O. Gropen, *Chem. Phys. Lett.* **286**, 261 (1998), URL <http://www.sciencedirect.com/science/article/pii/S0009261498001201>.
25. K. Andersson, P. Å. Malmqvist, B. O. Roos, A. J. Sadlej, and K. Wolinski, *J. Phys. Chem.* **94**, 5483 (1990), URL <http://dx.doi.org/10.1021/j100377a012>.
26. K. Andersson, P.-Å. Malmqvist, and B. O. Roos, *J. Chem. Phys.* **96**, 1218 (1992).
27. J. Finley, P.-Å. Malmqvist, B. O. Roos, and L. Serrano-Andrés, *Chem. Phys. Lett.* **288**, 299 (1998), URL <http://www.sciencedirect.com/science/article/pii/S0009261498002528>.
28. C. Angeli, R. Cimiraglia, S. Evangelisti, T. Leininger, and J.-P. Malrieu, *J. Chem. Phys.* **114**, 10252 (2001), URL <http://scitation.aip.org/content/aip/journal/jcp/114/23/10.1063/1.1361246>.
29. C. Angeli, R. Cimiraglia, and J.-P. Malrieu, *Chem. Phys. Lett.* **350**, 297 (2001), URL <http://www.sciencedirect.com/science/article/pii/S0009261401013033>.
30. C. Angeli, R. Cimiraglia, and J.-P. Malrieu, *J. Chem. Phys.* **117**, 9138 (2002), URL <http://scitation.aip.org/content/aip/journal/jcp/117/20/10.1063/1.1515317>.
31. C. Angeli, S. Borini, M. Cestari, and R. Cimiraglia, *J. Chem. Phys.* **121**, 4043 (2004), URL <http://scitation.aip.org/content/aip/journal/jcp/121/9/10.1063/1.1778711>.
32. D. Datta and M. Nooijen, *J. Chem. Phys.* **137**, 204107 (2012), URL <https://doi.org/10.1063/1.4766361>.
33. J. Brabec, K. Bhaskaran-Nair, N. Govind, J. Pittner, and K. Kowalski, *J. Chem. Phys.* **137**, 171101 (2012), URL <https://doi.org/10.1063/1.4764355>.

34. A. K. Dutta, J. Gupta, N. Vaval, and S. Pal, *J. Chem. Theory Comput.* **10**, 3656 (2014), URL <https://doi.org/10.1021/ct500285e>.
35. D. L. Yeager and P. Jørgensen, *Chem. Phys. Lett.* **65**, 77 (1979), URL <http://www.sciencedirect.com/science/article/pii/000926147980130X>.
36. E. Dalgaard, *J. Chem. Phys.* **72**, 816 (1980), URL <http://dx.doi.org/10.1063/1.439233>.
37. J. Olsen and P. Jørgensen, *J. Chem. Phys.* **82**, 3235 (1985).
38. P. Jørgensen, H. J. A. Jensen, and J. Olsen, *J. Chem. Phys.* **89**, 3654 (1988), URL <https://doi.org/10.1063/1.454885>.
39. B. Helmich-Paris, *J. Chem. Phys.* **150**, 174121 (2019), URL <https://doi.org/10.1063/1.5092613>.
40. O. Christiansen, P. Jørgensen, and C. Hättig, *Int. J. Quantum Chem.* **68**, 1 (1998).
41. S. Coriani, O. Christiansen, T. Fransson, and P. Norman, *Phys. Rev. A* **85**, 022507 (2012), URL <https://link.aps.org/doi/10.1103/PhysRevA.85.022507>.
42. A. Barth and J. Schirmer, *J. Phys. B: At. Mol. Opt. Phys.* **18**, 867 (1985).
43. J. Schirmer, *Phys. Rev. A* **26**, 2395 (1982).
44. S. Coriani and H. Koch, *J. Chem. Phys.* **143**, 181103 (2015), URL <https://doi.org/10.1063/1.4935712>.
45. M. Vidal, X. Feng, E. Epifanovsky, A. I. Krylov, and S. Coriani, *J. Chem. Theory Comput.* **15**, 3117 (2019), URL <https://doi.org/10.1021/acs.jctc.9b00039>.
46. S. D. George, T. Petrenko, and F. Neese, **361**, 965 (2008), URL <http://www.sciencedirect.com/science/article/pii/S0020169307003374>.
47. N. A. Besley and F. A. Asmuruf, *Phys. Chem. Chem. Phys.* **12**, 12024 (2010), URL <http://dx.doi.org/10.1039/C002207A>.

48. F. A. Asmuruf and N. A. Besley, Chem. Phys. Lett. **463**, 267 (2008), URL <http://www.sciencedirect.com/science/article/pii/S0009261408011469>.
49. R. B. Morgan, Linear Algebra Appl. **154-156**, 289 (1991), URL <http://www.sciencedirect.com/science/article/pii/0024379591903816>.
50. R. B. Morgan and M. Zeng, Numer. Linear Algebr. **5**, 33 (1998).
51. D. R. Fokkema, G. L. G. Sleijpen, and H. A. Van der Vorst, SIAM J. Sci. Comput. **20**, 94 (1998), URL <https://doi.org/10.1137/S1064827596300073>.
52. E. Vecharynski and A. Knyazev, SIAM J. Sci. Comput. **37**, S3 (2015), URL <https://doi.org/10.1137/14098048X>.
53. D. Zuev, E. Vecharynski, C. Yang, N. Orms, and A. I. Krylov, J. Comput. Chem. **36**, 273 (2015), URL <https://onlinelibrary.wiley.com/doi/abs/10.1002/jcc.23800>.
54. J. M. Kasper, D. B. Williams-Young, E. Vecharynski, C. Yang, and X. Li, J. Chem. Theory Comput. **14**, 2034 (2018), URL <https://doi.org/10.1021/acs.jctc.8b00141>.
55. E. R. Davidson, J. Comput. Phys. **17**, 87 (1975).
56. A. R. Tackett and M. D. Ventra, Phys. Rev. B **66**, 245104 (2002), URL <https://link.aps.org/doi/10.1103/PhysRevB.66.245104>.
57. G. Jordan, M. Marsman, Y.-S. Kim, and G. Kresse, J. Comput. Phys. **231**, 4836 (2012), URL <http://www.sciencedirect.com/science/article/pii/S0021999112001829>.
58. J. J. Dorando, J. Hachmann, and G. K.-L. Chan, J. Chem. Phys. **127**, 084109 (2007), URL <https://doi.org/10.1063/1.2768360>.
59. A. Baiardi, C. J. Stein, V. Barone, and M. Reiher, J. Chem. Phys. **150**, 094113 (2019), URL <https://doi.org/10.1063/1.5068747>.
60. T. Helgaker, S. Coriani, P. Jørgensen, K. Kristensen, J. Olsen, and K. Ruud, Chem. Rev. **112**, 543 (2012).

61. T. Saue and H. J. A. Jensen, J. Chem. Phys. **118**, 522 (2003), URL <http://scitation.aip.org/content/aip/journal/jcp/118/2/10.1063/1.1522407>.
62. F. Neese, WIREs Comput. Mol. Sci. **2**, 73 (2012), URL <http://dx.doi.org/10.1002/wcms.81>.
63. F. Neese, WIREs Comput. Mol. Sci. **8**, e1327 (2018), URL <https://onlinelibrary.wiley.com/doi/abs/10.1002/wcms.1327>.
64. M. Douglas and N. M. Kroll, Ann. Phys.-New York **82**, 89 (1974), URL <http://www.sciencedirect.com/science/article/pii/0003491674903339>.
65. G. Jansen and B. A. Hess, Phys. Rev. A **39**, 6016 (1989), URL <https://link.aps.org/doi/10.1103/PhysRevA.39.6016>.
66. A. D. Becke, Phys. Rev. A **38**, 3098 (1988).
67. C. Lee, W. Yang, and R. G. Parr, Phys. Rev. B **37**, 785 (1988).
68. A. D. Becke, J. Chem. Phys. **98**, 5648 (1993).
69. G. L. Stoychev, A. A. Auer, and F. Neese, J. Chem. Theory Comput. **13**, 554 (2017), pMID: 28005364, URL <http://dx.doi.org/10.1021/acs.jctc.6b01041>.
70. N. B. Balabanov and K. A. Peterson, J. Chem. Phys. **123**, 064107 (2005), URL <http://dx.doi.org/10.1063/1.1998907>.
71. B. O. Roos, P. R. Taylor, and P. E. Siegbahn, Chem. Phys. **48**, 157 (1980), ISSN 0301-0104, URL <http://www.sciencedirect.com/science/article/pii/0301010480800450>.
72. G. J. Palenik, Inorg. Chem. **6**, 503 (1967), URL <https://doi.org/10.1021/ic50049a015>.
73. F. Weigend and R. Ahlrichs, Phys. Chem. Chem. Phys. **7**, 3297 (2005).
74. D. Pantazis, def2-QZVPP basis set contraction coefficients for the DKH2 Hamiltonian. Available in ORCA 4.0.

75. U. Arp, F. Federmann, E. Källne, B. Sonntag, and S. L. Sorensen, J. Phys. B: At. Mol. Opt. Phys. **25**, 3747 (1992).
76. B. Helmich-Paris, J. Chem. Theory Comput. **15**, 4170 (2019), URL <https://doi.org/10.1021/acs.jctc.9b00325>.
77. S. G. Minasian, J. M. Keith, E. R. Batista, K. S. Boland, J. A. Bradley, S. R. Daly, S. A. Kozimor, W. W. Lukens, R. L. Martin, D. Nordlund, et al., J. Am. Chem. Soc. **135**, 1864 (2013), URL <https://doi.org/10.1021/ja310223b>.
78. A. Y. Sokolov, J. Chem. Phys. **149**, 204113 (2018), URL <https://doi.org/10.1063/1.5055380>.
79. A. Köhn and A. Bargholz, J. Chem. Phys. **151**, 041106 (2019), URL <https://doi.org/10.1063/1.5115045>.

Figure 1: Schematic block structure of the full MC-TDA Hessian. Orbital rotations between the inactive, active, and virtual MO spaces are labeled V-O, A-O, and V-A. CI denotes the configuration part.

Figure 2: Schematic block structure of the CVS MC-TDA Hessian. For further details see Fig. 1 and text.

Figure 3: Relation between the eigenvalues of the original and the S&I eigenvalue problem. Eigenvalues close to shift s are relocated from the interior of the original eigenvalue spectrum to the exterior of the S&I eigenvalue spectrum.

Figure 4: Convergence of the minimum, maximum, and average residual Frobenius norm $||\mathbf{r}||$ of a 50 root CVS and S&I MC-RPA calculation. Convergence threshold for $||\mathbf{r}||$ was 10^{-4} . See text for further details.

Figure 5: O K-edge XA spectrum of MnO_4^- with S&I MC-RPA, CAS-CI, and NEVPT2. Dashed lines are experimental peak maxima of the $1s \rightarrow e^*$ and $1s \rightarrow t_2^*$ pre-edge transitions. A Gaussian broadening of 0.5 eV is employed which corresponds to the spectral resolution of the experimental spectrum given in Ref. 77.

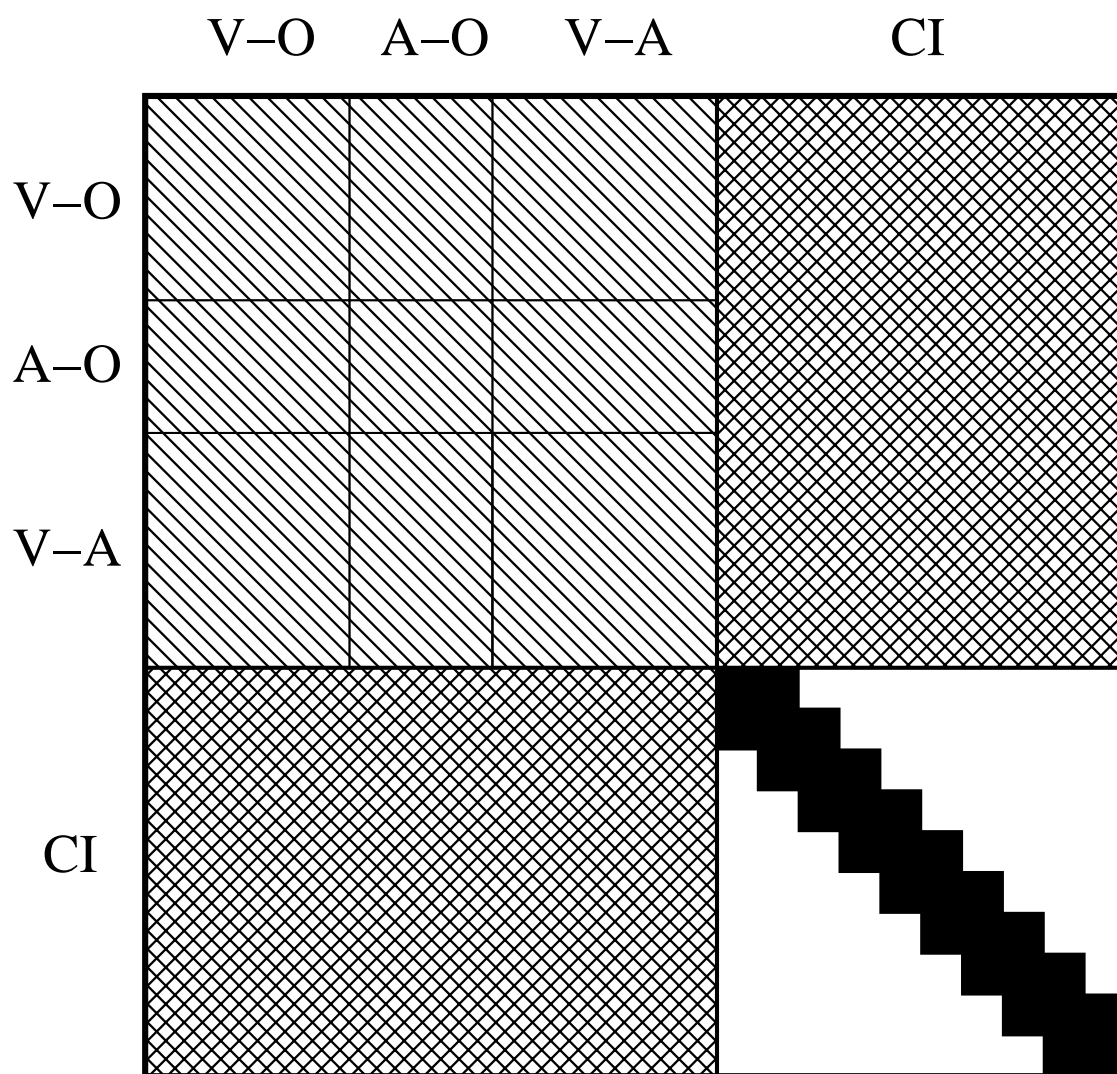


Figure 1
 B. Helmich-Paris
 Int. J. Quant. Chem.





	V-O	A-O	V-A	CI
V-O				
A-O				
V-A				
CI				

Figure 2
 B. Helmich-Paris
 Int. J. Quant. Chem.

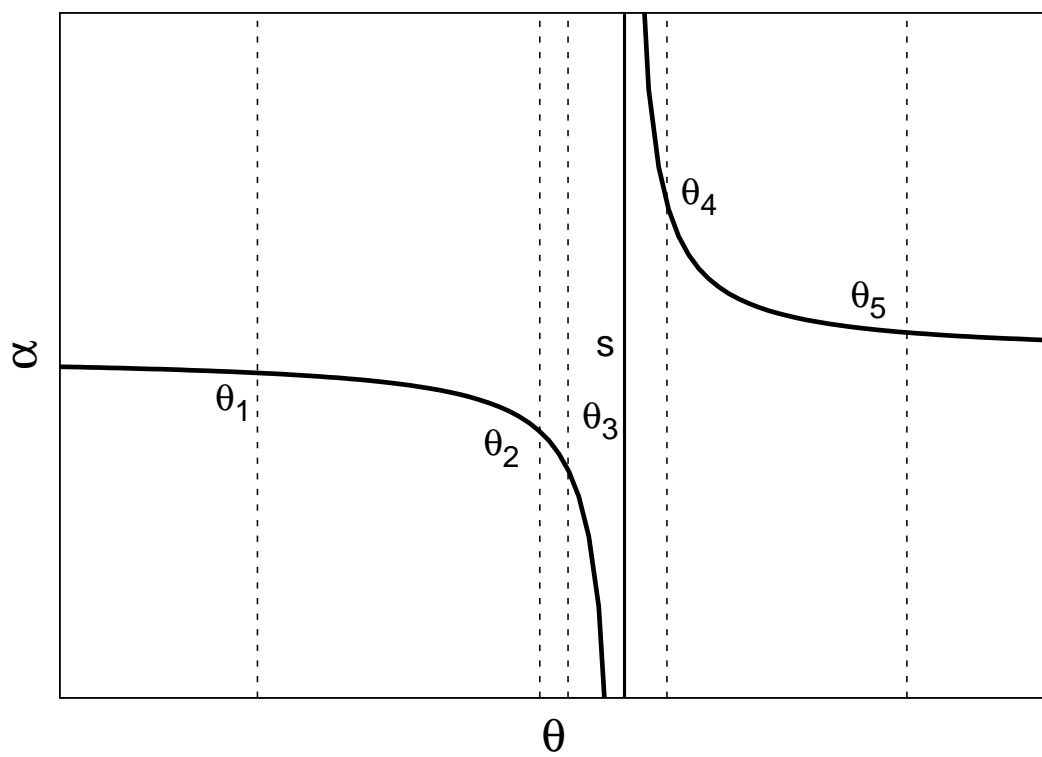


Figure 3
 B. Helmich-Paris
 Int. J. Quant. Chem.

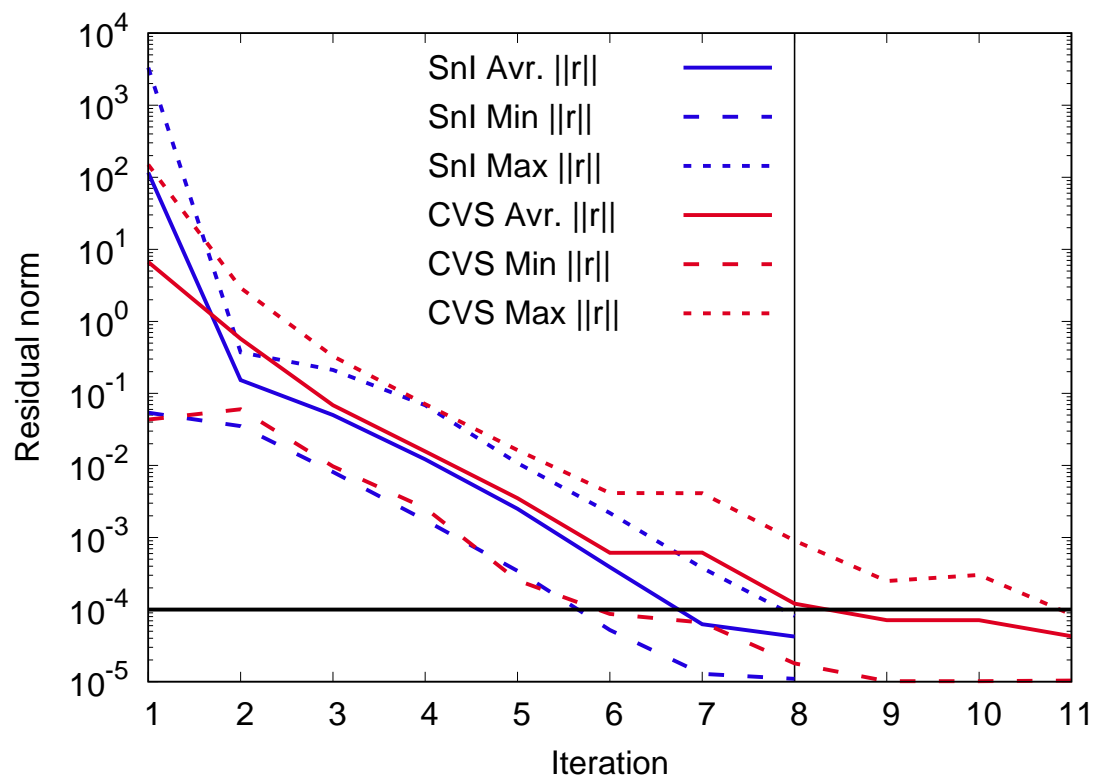


Figure 4
 B. Helmich-Paris
 Int. J. Quant. Chem.

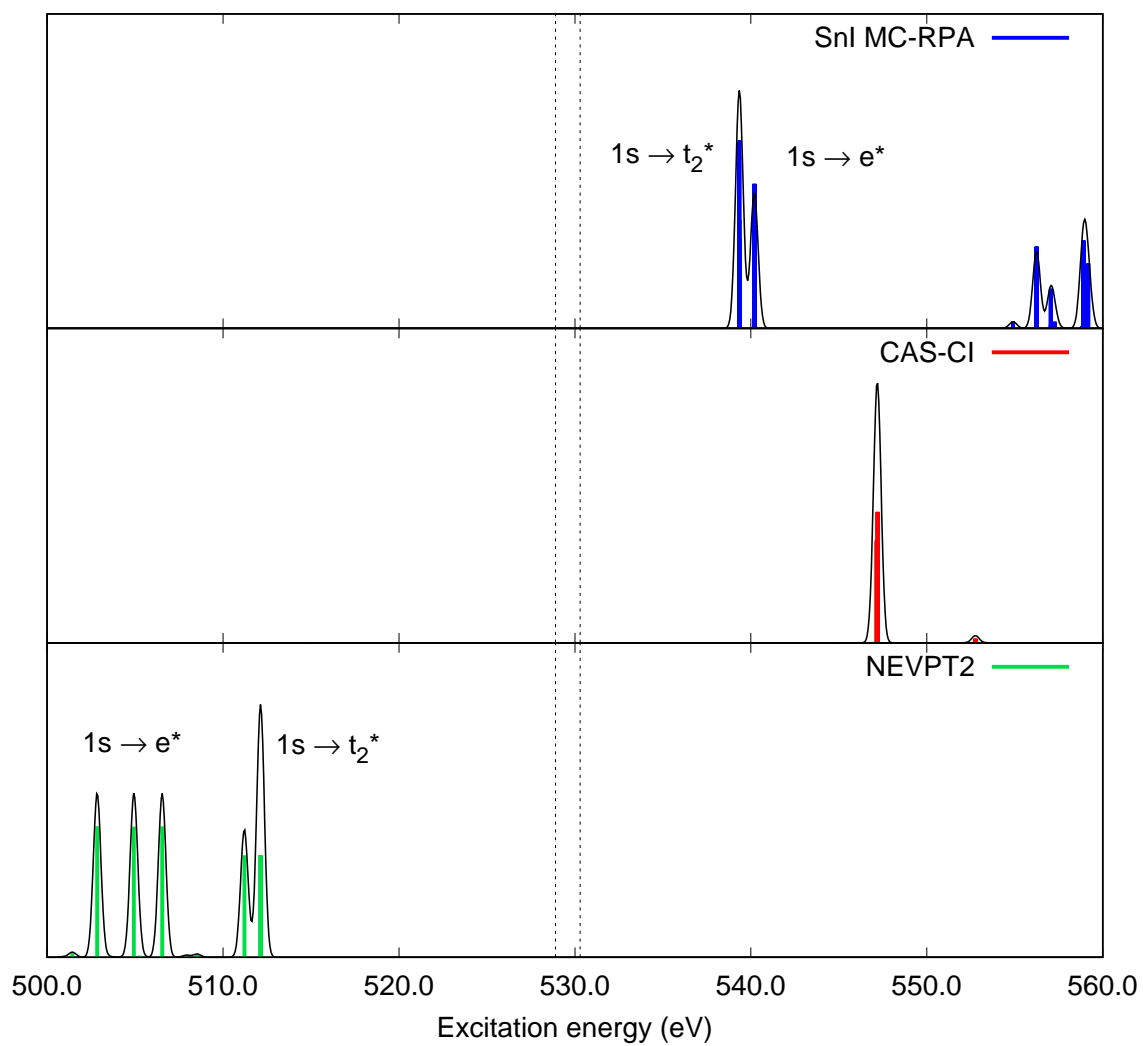


Figure 5
 B. Helmich-Paris
 Int. J. Quant. Chem.

State	Expt.	Methods					
		NEVPT2	$\Delta_{\text{CAS-CI}}$	Δ_{B3LYP}	$\Delta_{\text{CVS MC-RPA}}$	$\Delta_{\text{S\&I MC-RPA}}$	CVS - S\&I
K-edge							
6D	6545.88	6535.70	+40.67	-84.71	+39.82	+39.82	+1.2 10^{-4}
L-edge							
6F	/	640.87	+13.24	-11.02	+12.70	+12.67	+3.0 10^{-2}
6D	/	641.76	+13.35	-10.40	+12.86	+12.85	+4.5 10^{-3}
6P	/	642.96	+12.53	-7.61	+12.39	+12.40	-4.3 10^{-3}
M-edge							
6F	/	47.59	+0.58	-0.87	-0.16	-0.31	+1.5 10^{-1}
6D	/	48.64	+1.02	-1.21	+0.31	+0.30	+6.9 10^{-3}
6P	/	50.61	+3.66	+1.38	+1.99	-1.50	+3.5 10^0

Table 1: K-, L-, and M-edge XA transitions of the Manganese atom with different methods as well as the experimental K-edge are provided in eV. Differences Δ are given with respect to the NEVPT2 results. For further details see text.